analytical chemistry

pubs.acs.org/ac Article

Pt−Se-Bonded Nanoprobe for High-Fidelity Detection of Non-small Cell Lung Cancer and Enhancement of NIR II Photothermal Therapy

Zixuan Chang,[§] Tianrun Niu,[§] Qinghao Shao, Junming Yue, Hanbo Zhang, Lili Tong,* Xiaonan Gao,* and Bo Tang*

Cite This: *Anal. Chem.* 2023, 95, 18426−18435 Read Online

ACCESS | Metrics & More | Article Recommendations | Supporting Information

ABSTRACT: Non-small cell lung cancer (NSCLC) accounts for a high proportion of lung cancer cases globally, but early detection remains challenging, and insufficient oxygen supply at tumor sites leads to suboptimal treatment outcomes. Therefore, the development of core−shell Au@Pt−Se nanoprobes (Au@Pt−Se NPs) with peptide chains linked through Pt−Se bonds was designed and synthesized for NSCLC biomarker protein calcium-activated neutral protease 2 (CAPN2) and photothermal therapy (PTT) enhancement. The NP can be specifically cleaved by CAPN2, resulting in fluorescence recovery to realize the detection. The Pt−Se bonds exhibit excellent resistance to biologically abundant thiols such as glutathione, thus avoiding "false-positive" results and enabling precise detection of NSCLC. Additionally, the platinum (Pt) shell possesses catalase-like properties that catalyze the generation of oxygen from endogenous hydrogen peroxide within the tumor, thereby reducing hypoxia-inducible factor-1α (HIF-1α) levels and alleviating the hypoxic environment at the tumor site. The Au@Pt−Se NPs exhibit strong absorption bands, enabling the possibility of PTT in the near-infrared II region (NIR II). This study presents an effective approach for the early detection of NSCLC while also serving as an oxygen supplier to alleviate the hypoxic environment and enhance NIR II PTT.

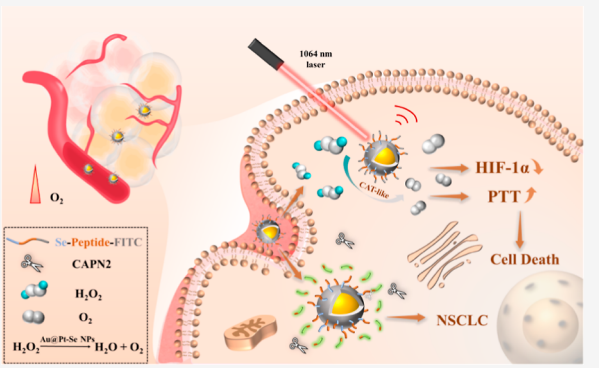

INTRODUCTION

Lung cancer is one of the most common types of cancer worldwide, which can be primarily classified into two types based on the distinct growth patterns of tumor cells: small cell lung cancer (SCLC) and non-small cell lung cancer (NSCLC).[1,2] NSCLC accounts for 85% of cases and is difficult to detect and diagnose in the early stages due to its slower growth and proliferation, as well as the lack of obvious warning signs.[3−5] Currently, common diagnostic methods for lung cancer include computed tomography, magnetic resonance imaging, and histopathological analysis. However, these techniques often present operational difficulties and are limited by their high costs.[6,7] Calcium-activated neutral protease 2 (CAPN2) is a calcium-dependent cysteine protease that plays a crucial role in angiogenesis, cell proliferation, and migration. Abnormal expression of CAPN2 has been observed in NSCLC, establishing it as a significant biomarker for NSCLC.[8] Hence, there is an urgent need to develop specific detection methods targeting CAPN2 to achieve early detection of NSCLC in order to realize early diagnosis and prognostic treatment for substantially enhancing the survival rate of patients.[9−13]

Hypoxia is a significant characteristic of the tumor microenvironment, where an imbalance between oxygen production and consumption results in oxygen deficiency in the tumor region.[14] The hypoxic microenvironment promotes tumor cell proliferation and migration while reducing their sensitivity to treatments, resulting in poor therapeutic outcomes.[15−17] Additionally, the metabolic dysfunction of tumor cells leads to a significant increase in endogenous hydrogen peroxide (H_2O_2) levels. Li's group utilized upconversion nanoparticles encapsulated in alginate microcapsules to achieve continuous oxygen generation in vivo, thereby alleviating the tumor's hypoxic environment.[18] Currently, the primary treatment methods for lung cancer include surgery, chemotherapy, and radiation therapy, but these approaches often have strong side effects. Therefore, photothermal therapy (PTT) has gradually gained attention as an alternative cancer treatment strategy.[19,20] PTT offers the advantages of precision, safety, and effectiveness through the use of high-energy laser beams to heat tissue, making it a promising and beneficial treatment approach. With the extension of the near-infrared II wavelength range (1000−1350 nm), which exhibits deep tissue penetration and minimal

Received: August 6, 2023
Revised: November 19, 2023
Accepted: November 20, 2023
Published: December 5, 2023

Scheme 1. (A) Schematic Diagram of the Synthesis Pathways for Au Nanoparticles, Au@Pt NPs, and Au@Pt−Se NPs, as well as the Specific Cleavage of Au@Pt−Se NPs by the CAPN2 Protein, Leading to Fluorescence Recovery[a]

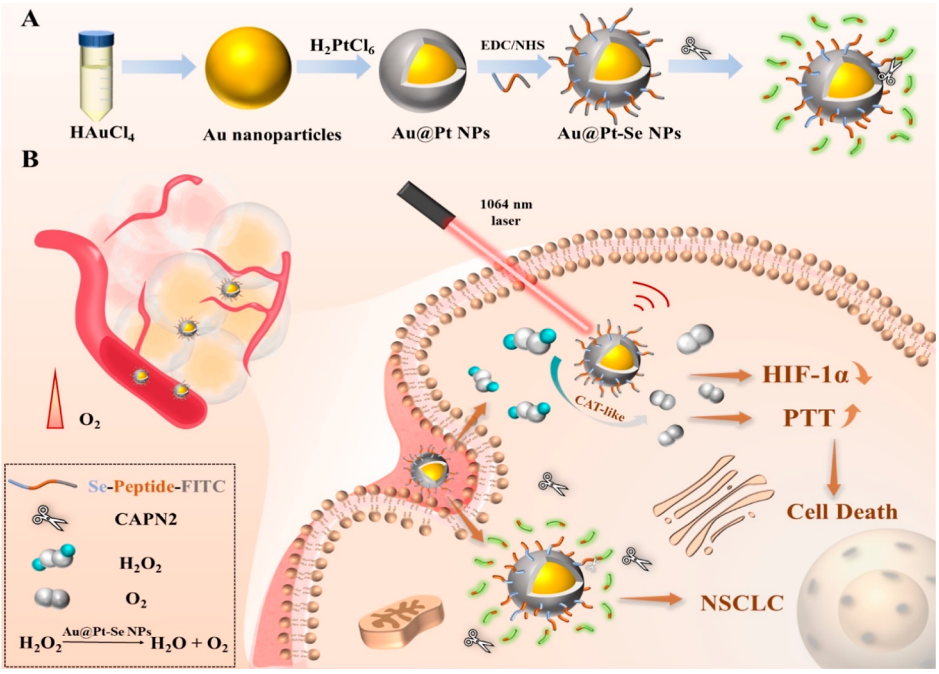

[a](B) Illustration of the effects of Au@Pt−Se NPs in NSCLS cells. Au@Pt−Se NPs catalyze the generation of O_2 from endogenous H_2O_2, alleviating the hypoxic environment, reducing hypoxia-inducible factor-1α (HIF-1α) levels, and enhancing PTT. Additionally, they enable detection of NSCLC within the cells.

photon scattering, PTT has evolved from the initial NIR I region to the NIR II region.[21−25]

Nanomaterials exhibit excellent properties in terms of size, biocompatibility, and in vivo retention time.[26] Au nanoparticles are commonly used for the detection of certain cancer biomarkers due to their great biocompatibility, easy functionalization, and surface plasmon resonance properties. Our group discovered that the Au−Se bond possesses significant resistance to interference from biological thiols, enabling detection of various cancers, such as prostate cancer.[27−29] In recent years, materials based on Pt have attracted considerable attention due to low ligand exchange rates, high ligand stability, and strong Pt−Se bond strength.[30−32] These characteristics give Pt−Se-based NPs a natural advantage in resisting endogenous thiols in biological systems. Moreover, Pt exhibits excellent catalase-like activity, catalyzing the generation of O_2 from H_2O_2. Additionally, Pt possesses the potential for tunable localized surface plasmon resonance resulting from collective electron oscillation and exhibits a self-heating effect through electron−phonon scattering. Therefore, O_2 generated by Pt alleviates the hypoxic microenvironment inside cells and significantly enhances the PTT effect, making it an effective photothermal agent.[33−36]

Herein, in this work, novel core−shell Au@Pt−Se nanoprobes (Au@Pt−Se NPs) were designed and synthesized. The specific peptide chain targeting CAPN2, with fluorescein isothiocyanate (FITC) modified at the terminal and selenothiol modified at the top, was connected to the Pt shell via the Pt−Se bond. The peptide chain can be specifically cleaved by CAPN2 protein, causing the fluorescent group to detach from the surface of the Au@Pt NPs and restoring the fluorescence by eliminating the fluorescence resonance energy transfer effect, thereby enabling specific detection of NSCLS. Simultaneously, the Pt shell structure can catalyze the generation of O_2 from H_2O_2 inside cells, alleviating the hypoxic environment at the tumor site and reducing the expression of the intracellular HIF-1α.[37,38] Furthermore, utilizing the excellent photothermal effect of Pt, under laser irradiation at NIR II wavelength, the Au@Pt−Se NPs convert light energy into heat energy, achieving effective PTT (Scheme 1).

RESULTS AND DISCUSSION

Au nanoparticles were prepared using the classical sodium citrate reduction method,[39] followed by the reduction of chloroplatinic acid in the prepared Au nanoparticle solution. Transmission electron microscopy (TEM) analysis revealed that both synthesized Au nanoparticles and Au@Pt NPs exhibited uniform spherical shapes with decent dispersion (Figure 1A,B). The core−shell structure enveloped by the Pt shell can be observed by high-resolution TEM (HRTEM), with the Pt shells' thickness of approximately 2 nm (Figure 1C), indicating that Pt did not erode the Au nanoparticles but underwent reduction on their surfaces. The sizes of Au nanoparticles and Au@Pt NPs were measured to be 13.0 ± 0.5 and 15.0 ± 0.7 nm, respectively, which were consistent with dynamic light scattering (DLS) measurements (Figure 1D,E). Moreover, elemental mapping analysis demonstrated the overlapping distribution of Au and Pt elements on the surface of Au nanoparticles, confirming the coexistence of Au and Pt on Au@Pt NPs and the successful formation of a core−shell structure (Figures 2A and S1). Additionally, UV−visible (UV−vis) spectroscopy analysis showed that the absorption peak of Au nanoparticles was around 520 nm, while the absorption peak of Au@Pt NPs shifted to 511 nm, indicating a significant blue shift in the UV−vis absorption peak and a color change

https://doi.org/10.1021/acs.analchem.3c03511
Anal. Chem. 2023, 95, 18426−18435

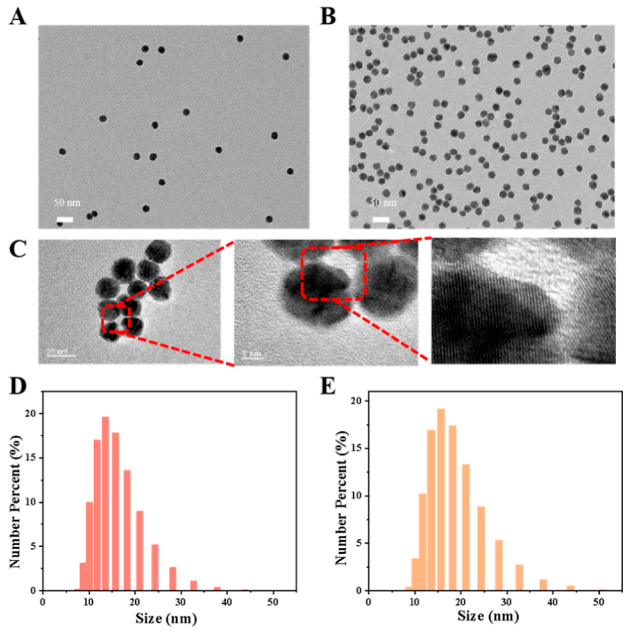

Figure 1. TEM images of (A) Au nanoparticles and (B) Au@Pt NPs. (C) HRTEM images of Au@Pt NPs and their lattice fringes. DLS images of (D) Au nanoparticles and (E) Au@Pt NPs.

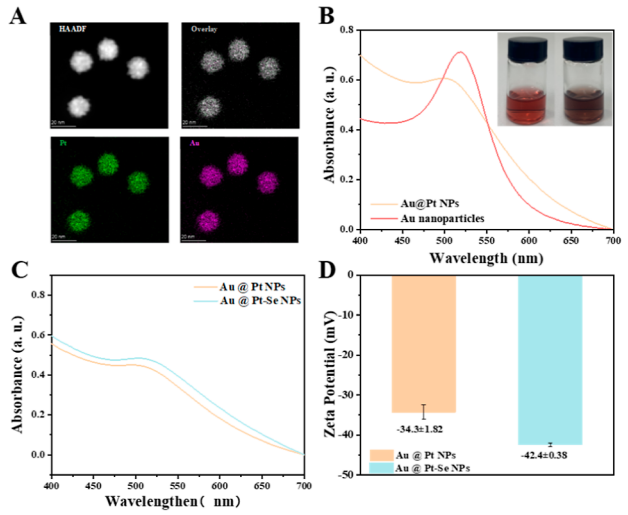

Figure 2. (A) Elemental mapping images of Au@Pt NPs. (B) UV−vis absorption of (red) Au nanoparticles and (orange) Au@Pt NPs, with an inset of corresponding pictures. (C) UV−vis absorption of (orange) Au@Pt NPs and (blue) Au@Pt−Se NPs. (D) Zeta potential of (orange) Au@Pt NPs and (blue) Au@Pt−Se NPs.

from burgundy to brownish, proving the reaction between chloroplatinic acid and Au nanoparticles (Figure 2B). These experiments collectively confirmed the successful synthesis of Au@Pt NPs.

The Au@Pt−Se NPs were synthesized via peptide modification method,[40] which coupled the −COOH end of the obtained peptide chain with the $-NH_2$ end of selenocysteine to obtain an intermediate (FITC-CAPN2-Cys-Se-Se-Cys-CAPN2-FITC). After breaking the diselenide bond under light conditions, the peptides were connected to Au@Pt NPs, resulting in CAPN2-specific NPs based on the Pt−Se bond. Consistent with TEM results, the size distribution of the modified NPs increases to 17.0 ± 0.4 nm compared to the previous Au@Pt NPs (Figures S2 and S3), which is due to the successful modification of peptide chains. The UV−vis absorption peak shifted from 511 to 515 nm (Figure 2C), displaying a broader absorption, suggesting that Au@Pt−Se NPs may convert light energy into heat under NIR II laser irradiation. Subsequently, zeta potential was performed, which changed from −34.3 ± 1.82 to −42.4 ± 0.38 eV (Figure 2D), indicating the successful modification of the peptide chain on the NPs' surface due to the increased carboxyl groups introduced by the peptide chain. These experiments confirm the successful modification of the peptide chain on Au@Pt NPs through the Pt−Se bond.

Furthermore, the loading capacity of the peptide chain on Au@Pt NPs was quantified. The fluorescence intensity of FITC-modified peptide chains at different concentrations was measured to obtain a standard fluorescence curve for the peptide chain under the same selenocysteine concentration, ion strength, and pH conditions (Figure S4). The Au@Pt−Se NPs were diluted to a final concentration of 1 nM, and an excess of selenocysteine (Sec) was used to replace the peptide chain. The supernatant was collected after centrifugation for the fluorescence analysis (Figure 3A). By comparing the

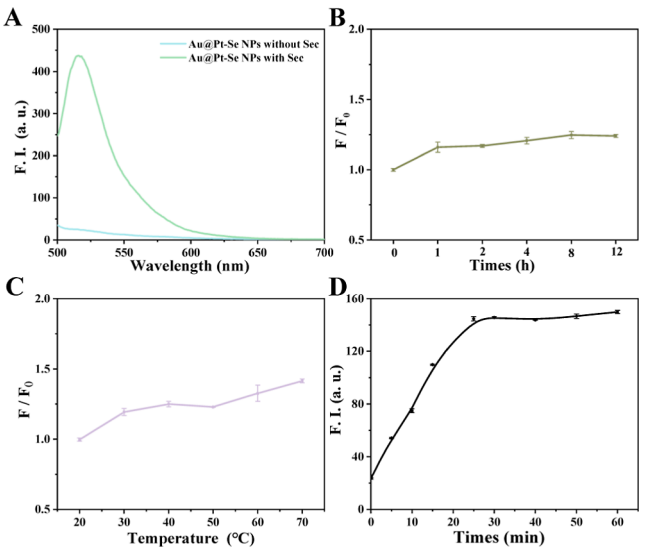

Figure 3. (A) Fluorescence intensity images of (green) Au@Pt−Se NPs replaced with selenocysteine and (blue) Au@Pt−Se NPs. (B) NP's performance at different time points under 5 nM GSH. (C) Fluorescence changes of Au@Pt−Se NPs with temperature. (D) Kinetic response of Au@Pt−Se NPs to CAPN2 protein.

obtained fluorescence intensity with the standard calibration curve of FITC-labeled peptide chains ($Y = 3.54X + 34.86$), the total concentration of the peptide chain was calculated and then divided by the concentration of NPs to determine the number of peptide chains connected to each Au@Pt NP, resulting in an average number of 154 ± 2. This indicates that the NPs sufficiently load peptide chains, ensuring a promising fluorescence recovery rate in the subsequent experiments.

The stability of Au@Pt−Se NPs in the presence of different concentrations of glutathione (GSH) was first examined. When the NPs' and GSH concentrations were, respectively, 1 and 5 mM, the NPs were incubated for different durations (0, 1, 2, 4, 8, and 12 h). Despite the increase in incubation time, the fluorescence contrast remained relatively constant and showed minimal variation over time (Figure 3B). The NPs

https://doi.org/10.1021/acs.analchem.3c03511
Anal. Chem. 2023, 95, 18426−18435

were then incubated for 12 h in solutions containing different GSH concentrations (0, 10, 50, 100, 200, 500, 1000, and 5000 μM).

Under the same incubation time, the fluorescence contrast showed only slight changes with increasing GSH concentration (Figure S5), demonstrating that the influence of GSH concentration on the fluorescence intensity of the probe, in the absence of the target protein, can be considered negligible. Therefore, despite variations in GSH concentration and incubation time, the fluorescence contrast of the NPs remained relatively constant, suggesting that the NPs' fluorescence recovery was not significantly affected by GSH. In this regard, the Pt−Se bond possesses excellent resistance to GSH and can minimize "false-positive" signals of the NPs. Further investigation of the stability of Au@Pt−Se NPs under different temperatures was conducted by incubating the probe at various temperatures (20, 30, 40, 50, 60, and 70 °C) for 5 min. No significant change in fluorescence contrast intensity with increasing temperature (Figure 3C) was observed, proving the NPs' thermal stability within a wide temperature range, which provides possibilities for subsequent PTT. These results indicate that the Pt−Se bond owns excellent stability to avoid "false-positive" signals caused by GSH and lays the foundation for further cellular experiments. Au@Pt−Se NPs (1 nM) were incubated with CAPN2 at 37 °C for various durations to determine the optimal response time of the NPs. The fluorescence intensity gradually increased as the incubation time between Au@Pt−Se NPs and the protein (0, 10, 20, 30, 40, 50, and 60 min) was prolonged. Simultaneously, the optimal excitation and emission wavelengths of the probe in response to CAPN2 were obtained (Figures 3D and S6). The fluorescence intensity reached its plateau at 35 min and remained relatively constant thereafter. Consequently, the optimal response time of the NPs to CAPN2 was established to be 35 min, and the optimal excitation and emission wavelengths were found to be, respectively, 480 and 520 nm, which were used in subsequent experiments.

The UV−vis absorption spectra of different concentrations of H_2O_2 were first established with a standard linear calibration curve at 240 nm (R^2 = 0.9994) (Figures 4A and S7). The NPs reacted with an excess of H_2O_2 (20 mM) at different time intervals, and their UV−vis absorption spectra were measured. The NPs were found to completely consume excess H_2O_2 within 25 min (Figure 4B), indicating their ability to deplete H_2O_2 over a certain period of time. In the control group without NPs, the UV−vis absorption spectra showed that H_2O_2 itself can remain stable within 60 min (Figure S8), ruling out the possibility of self-decomposition during the experiment. These findings suggest that Au@Pt−Se NPs have the capability of catalyzing the consumption of H_2O_2. The catalytic capability of the NPs to generate O_2 from H_2O_2 was examined. First, there is significant bubble production when H_2O_2 and Au@Pt−Se NPs are mixed (Figure S9). Due to the rapid reaction between the 1 nM probe and excess H_2O_2 (20 mM), a lower concentration of the probe (0.15 nM) in combination with excess H_2O_2 (20 mM) was chosen and measured by a sensitive oxygen probe $[Ru(DPP)_3]Cl_2$ (RDPP). RDPP probe (0.5 μM) was separately incorporated into Au@Pt−Se NPs, H_2O_2, H_2O, and a combination of the probe and H_2O_2 (Figure 4C). The fluorescence intensity of the RDPP probe remained stable in H_2O and the NPs solution while exhibiting a slight decrease in the presence of H_2O_2. This minor decrease in fluorescence intensity may be attributed to the decomposition

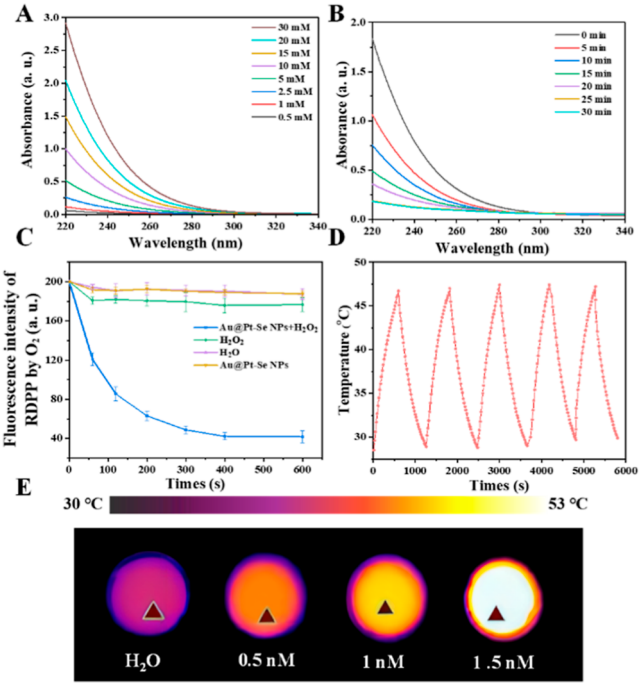

Figure 4. (A) UV−vis spectra of H_2O_2 at different concentrations. (B) UV−vis spectra of the reaction between residual H_2O_2 and Au@Pt−Se NPs at different time intervals. (C) Fluorescence intensity decay of RDPP in H_2O_2 solution (20 mM) catalyzed by Au@Pt−Se NPs (0.15 nM) compared to H_2O, H_2O_2, or Au@Pt−Se NPs (0.15 nM). (D) Time-dependent temperature changes of the Au@Pt−Se NPs (1 nM) aqueous solution under cyclic irradiation with a 1064 nm laser (1.8 W/cm^2) for five cycles. (E) Infrared images of aqueous solutions containing different concentrations of Au@Pt−Se NPs after 10 min of treatment with 1064 nm laser irradiation (1.8 W/cm^2).

of H_2O_2 by the laser in the fluorometer, resulting in the generation of O_2 and a subsequent slight decrease in the fluorescence intensity of the RDPP probe. Notably, the fluorescence intensity of the RDPP probe significantly decreased when combined with H_2O_2, reaching a plateau after 400 s. Such an observation aligns with the results obtained by measuring the O_2 content in the solution using a dissolved O_2 meter during the reaction between the probe and H_2O_2 (Figure S10). Moreover, at 400 s, the O_2 content in the solution reached 43.2 mg/mL, indicating the efficient catalytic capacity of Au@Pt−Se NPs in generating O_2 from H_2O_2 within a short time frame. This property suggests the potential of the probe to improve the hypoxic tumor microenvironment.

By measuring the UV−vis−NIR spectra of NPs at different concentrations (0.5, 1, and 1.5 nM), it was observed that a broad absorption band was exhibited at the NIR II wavelength, indicating that the core−shell structure of Au@Pt could efficiently convert light energy into heat within the NIR II window (Figure S11). Heat generation of the NPs at different concentrations (0.5, 1, and 1.5 nM) was conducted to testify to the NPs' photothermal effect. When the NPs' concentration was set to be 1 nM, under 1064 nm laser irradiation (1.8 W/cm^2) for 10 min, the solution temperature rose from room temperature (25.6 °C) to approximately 48 °C, indicating the NPs' excellent photothermal effects. To further examine whether the NPs can sustain heat generation, 1 nM NPs was subjected to five cycles of 1064 nm laser irradiation It was found that the NPs maintained high sensitivity to the laser even after multiple heating cycles. The heat generation

https://doi.org/10.1021/acs.analchem.3c03511
Anal. Chem. 2023, 95, 18426−18435

capability of the NPs did not decrease but instead achieved the desired temperature of around 48 °C slightly faster (Figures 4D,E and 5A). These findings demonstrate that Au@Pt−Se

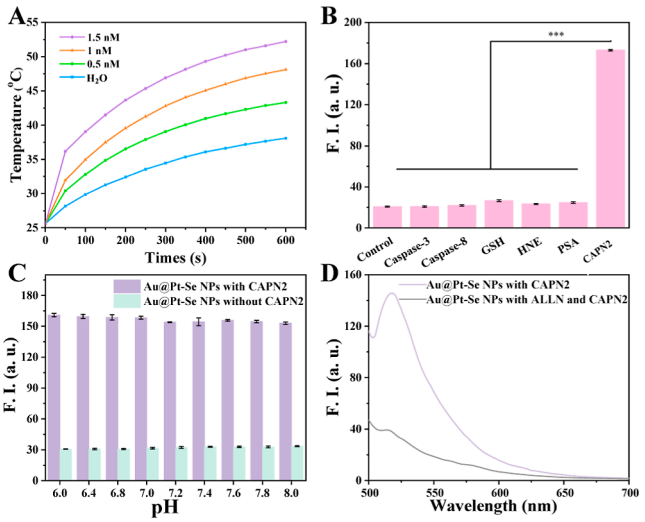

Figure 5. (A) Temperature variation of aqueous solutions containing different concentrations of Au@Pt−Se NPs under 1064 nm laser irradiation for 10 min (1.8 W/cm^2). (B) Fluorescence recovery profiles of Au@Pt−Se NPs' selective response to CAPN2 compared to other proteins in a simulated physiological environment, ***P < 0.001. (C) Fluorescence intensities of (blue) the Au@Pt−Se NPs' stability at different pH values and (purple) the response of Au@Pt−Se NPs to CAPN2 at different pH values. (D) Fluorescence recovery profiles of Au@Pt−Se NPs (black) in the presence of CAPN2 inhibitor ALLN and (purple) in the presence of CAPN2 alone in a simulated physiological environment.

NPs have effective photothermal properties in an extracellular environment, which makes them a promising candidate for future applications in intracellular NIR-II PTT therapy.

The NPs' stability over a wide pH range and their specificity toward the target protein CAPN2 are crucial for application. Under simulated physiological conditions within the pH range of 6.0−8.0 (6.0, 6.4, 6.8, 7.0, 7.2, 7.4, 7.6, 7.8, and 8.0), the fluorescence of the control group probe did not exhibit significant changes, which indicates that the probe remained stable within such pH range. However, upon addition of the target protein CAPN2, there was a certain degree of fluorescence recovery, and the difference in fluorescence response among different pH values was not significant (Figure 5B). Hence, the probe owns great pH stability and detection ability of the target protein CAPN2 within a wide pH range, suggesting that pH does not have a significant impact on the utilization of this probe and further implies its potential suitability for complex and variable physiological environments. Next, the NPs were diluted to a final concentration of 1 nM in Tris−HCl (10 mM, pH = 7.4), and different concentrations of CAPN2 (25, 200, 400, 600, 800, and 1000 ng/mL) were added to the solution. The mixture was then incubated at 37 °C for 35 min, and a good linear response relationship was proved by the standard calibration curve (R^2 = 0.999) (Figure S12). Furthermore, the detection limit was determined to be 1.459 ng/mL, indicating that the probe exhibits good sensitivity toward CAPN2 and can be used for quantitative detection. The fluorescence intensity of the other groups was similar to that of the control group without any protein, indicating that the NPs specifically responded to CAPN2, with minimal interference from other protein types (Figure 5C). Further investigation of the NPs' specificity to CAPN2 protein was conducted using the CAPN2 protein activity inhibitor ALLN. It can be observed that there was minimal fluorescence recovery in the ALLN group, but the control group without the inhibitor showed normal fluorescence recovery (Figure 5D), which further confirms that the NPs' fluorescence recovery is achieved by CAPN2.

Before the response of Au@Pt−Se NPs to intracellular CAPN2 protein was studied, the cytotoxicity of the probe was evaluated through an MTT assay using A549 cells. The cells were divided into two groups and cultured with the medium containing a final concentration of 1 nM of Au@Pt−Se NPs or Au@Pt NPs, while keeping other conditions of cell culture constant (Figure 6A). The cell viability remained above 80%

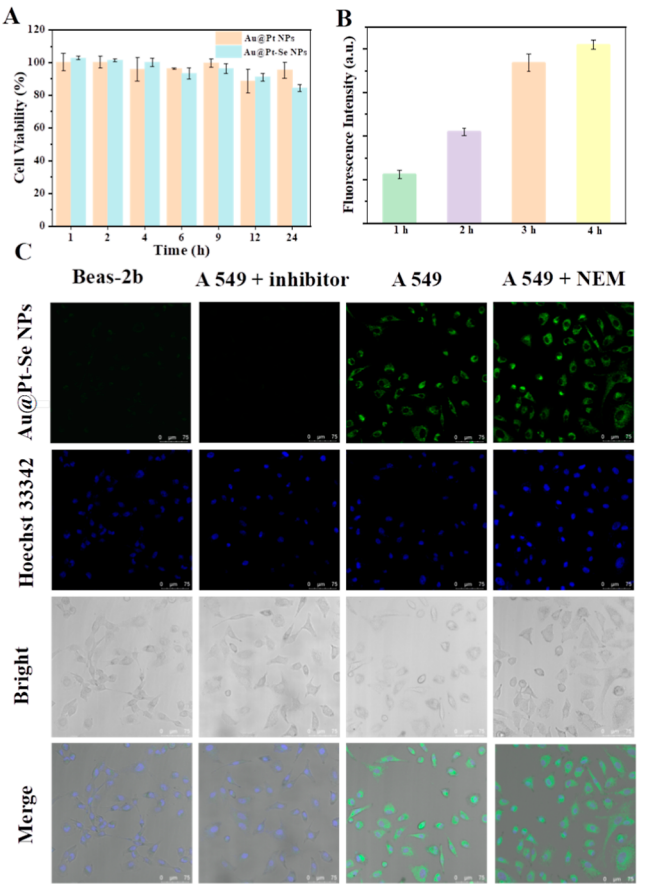

Figure 6. (A) In vitro cell toxicity evaluation of (orange) Au@Pt NPs and (blue) Au@Pt−Se NPs with A549 cells using the MTT assay. (B) Quantitative analysis of fluorescence intensity of Au@Pt−Se NPs taken up by A549 cells at different time points. (C) Fluorescence distribution images of Beas-2b cells, A549 cells treated with CAPN2 inhibitor ALLN, A549 cells, and A549 cells treated with NEM treated with Au@Pt−Se NPs.

even with an increased incubation time, indicating negligible cytotoxicity of both Au@Pt−Se NPs and Au@Pt NPs. These results demonstrate the excellent biocompatibility of the probe, allowing its use in subsequent cell experiments. Moreover, the cellular uptake of Au@Pt−Se NPs was explored by measuring the fluorescence intensity of the intracellular probe. To better localize the cells and avoid background interference, the cells were first activated using the calcium ionophore (ionomycin)

https://doi.org/10.1021/acs.analchem.3c03511
Anal. Chem. 2023, 95, 18426−18435

to induce the expression of the intracellular CAPN2 protein. After coincubation of the NPs with the cells, Hoechst 33342 was used to stain the cell nuclei, facilitating cell localization. Confocal laser scanning microscopy (CLSM) results revealed that the fluorescence intensity inside the cells increased in a time-dependent manner with the duration of probe-cell coincubation (Figures 6B and S13). Within 3 h, the fluorescence intensity inside the cells gradually increased. At 4 h, the fluorescence intensity inside the cells did not show a significant increase compared to the intensity at 3 h, indicating that cellular uptake of the probe reached saturation at 4 h. This observation is supported by the quantification of fluorescence intensity and demonstrates the NPs' excellent biocompatibility and its favorable internalization by the cells. Therefore, for subsequent cell experiments, a 4 h coincubation period was chosen as the optimal incubation time. By comparing NPs-treated fluorescence intensity between Beas-2b cells, A549 cells, and A549 cells with ALLN, the Beas-2b cells and A549 cells with ALLN both exhibited a weak fluorescence signal. However, A549 cells without the inhibitor ALLN displayed a strong fluorescence signal, illustrating a significant difference in fluorescence intensity between the A549 cells and the other two groups (***$P < 0.001$). Additionally, *N*-ethylmaleimide (NEM) was employed as a thiol-cleaving agent, and no significant fluorescence changes in Au@Pt−Se NPs before and after NEM treatment were observed (Figures 6C and S14). This indicates the NPs' excellent stability ex vivo, which makes them capable of specifically detecting CAPN2 in the NSCLS cells.

The fluorescence intensity of the intracellular RDPP probe was used to reflect the oxygen content within the cells under hypoxic conditions (1% O_2). Four groups, blank control, Au@Pt−Se NPs, H_2O_2, and Au@Pt−Se NPs with H_2O_2 were set to incubate with the cells under hypoxic conditions (Figure 7A,B). The cells were treated with an RDPP probe (15 μM) for 30 min, followed by cell imaging using CLSM. Compared to the blank control, both the Au@Pt−Se NPs group and the H_2O_2 group did not show a significant decrease in intracellular fluorescence intensity. However, the fluorescence intensity of RDPP significantly decreased in the Au@Pt−Se NPs with the H_2O_2 group (*$P < 0.05$), indicating that the O_2 generated by the catalysis of Au@Pt−Se NPs on H_2O_2 can turn off the fluorescence of RDPP. Furthermore, the level of the HIF-1α in the cells was further examined by ELISA kits under normoxic (21%) condition with the NPs, hypoxic (1%) condition with the NP, and hypoxic (1%) condition with the NPs and H_2O_2 (Figure 7C,D). Only the cells treated with the NPs and H_2O_2 showed a significant decrease in the concentration of the HIF-1α compared to the other two groups (**$P < 0.01$). Western blot analysis displayed similar results; under hypoxic conditions, the bands of cells cotreated with the NPs and H_2O_2 appeared lighter compared to the only NP group. These experiments collectively demonstrate that the NPs can catalyze H_2O_2, leading to the in situ generation of O_2, which in turn reduces the level of expression of HIF-1α within the cells. Furthermore, the NPs significantly improve the hypoxic environment at the tumor site, thereby enhancing the sensitivity of tumor cells to treatment and improving the effectiveness of PTT.

In order to evaluate the PTT effect of Au@Pt−Se NPs in vitro, six groups under hypoxic conditions (1% O_2) were set as follows: blank control, H_2O_2 (100 μM), 1064 nm laser irradiation (1.8 W/cm^2, 10 min), Au@Pt−Se NPs, Au@Pt−Se NPs and 1064 nm laser irradiation (1.8 W/cm^2, 10 min), and Au@Pt−Se NPs with H_2O_2 (100 μM) and 1064 nm laser irradiation (1.8 W/cm^2, 10 min) (Figure 8A). Additionally, five groups under normoxic conditions were also set: blank control, H_2O_2 (100 μM), 1064 nm laser irradiation (1.8 W/cm^2, 10 min) group, Au@Pt−Se NPs, and Au@Pt−Se NPs with H_2O_2 (100 μM) and 1064 nm laser irradiation (1.8 W/cm^2, 10 min) (Figures S15 and S16). Unlike previous results, the cells were not activated with the calcium ion carrier ionomycin before probe incubation to avoid interference from the NPs' green fluorescence in the subsequent staining process. Subsequently, live cells (stained green) and dead cells (stained red) were double stained with AM/propidium iodide (PI) for 30 min, and imaging was performed using CLSM. Under hypoxic conditions (1% O_2), the NPs with H_2O_2 and laser group showed a significant increase in cell death, and the cell death rate was significantly higher compared to those of other groups. Moreover, the NPs with H_2O_2 and laser group exhibit similar cell death rates in both hypoxic and normoxic conditions, proving the NPs catalyze the generation of oxygen from H_2O_2 degradation, thereby improving the hypoxic environment for enhancing the PTT effect in tumor cells. Cellular apoptosis rates were further assessed using flow cytometry, and the results were consistent with those obtained through CLSM (Figures 8B and S17), which further confirmed the therapeutic effect of the NPs on tumor cells.

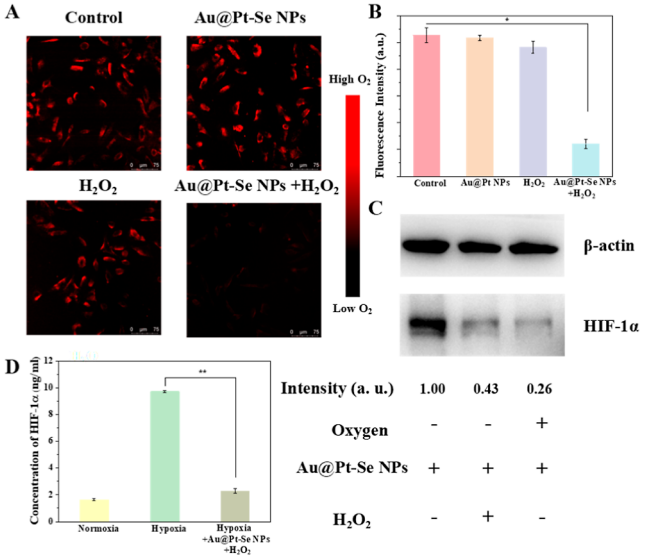

Figure 7. (A) Fluorescence images of RDPP intensity in A549 cells under hypoxia (1% O_2) after different treatments (untreated control, H_2O_2, Au@Pt−Se NPs, or Au@Pt−Se NPs + H_2O_2), indicating intracellular O_2 levels. *$P < 0.05$. (B) Quantification of RDPP intensity fluorescence images using ImageJ after different treatments (untreated control, H_2O_2, Au@Pt−Se NPs, or Au@Pt−Se NPs + H_2O_2). (C) Immunoblot analysis of HIF-1α protein levels after different treatments, with β-actin as the control. Quantification of band density was performed using ImageJ. (D) Quantitative analysis of HIF-1α concentration after different treatments using ELISA kits. **$P < 0.01$.

CONCLUSIONS

In summary, a novel core−shell structure of Au@Pt−Se NPs was designed and synthesized for early diagnosis of NSCLC. Such NPs can be specifically cleaved by the NSCLC-specific biomarker CAPN2 protein, leading to fluorescence recovery

https://doi.org/10.1021/acs.analchem.3c03511
Anal. Chem. 2023, 95, 18426−18435

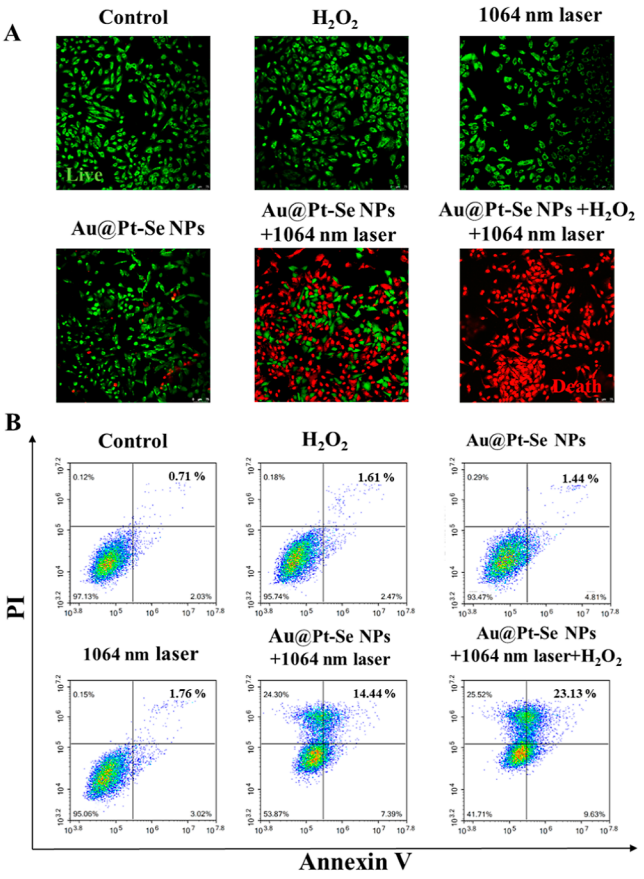

Figure 8. (A) Fluorescence images of A549 cells under hypoxic conditions stained with (green) live and (red) dead cell staining cells treated with different interventions, and the images were captured after 10 min of 1064 nm laser irradiation. (B) Flow cytometry analysis of apoptosis in A549 cells under hypoxic conditions using Annexin-V/PI staining. The quadrants represent healthy cells, early apoptotic cells, late apoptotic cells, and necrotic cells in a counterclockwise direction.

and enabling specific and accurate detection. Moreover, the Pt−Se bonds exhibit excellent resistance to interference from biological thiols, thereby avoiding "false-positive" results and achieving high-fidelity detection. Additionally, by leveraging the catalytic ability of Au@Pt−Se NPs to generate oxygen from endogenous H_2O_2 and their efficient photothermal effect, the hypoxic environment at the tumor site can be improved, enhancing the PTT effect in the NIR II region. The developed Au@Pt−Se NPs provide a new approach for clinical early detection, diagnosis, and combined PTT of NSCLC, offering new insights and potential applications for future lung cancer detection and treatment.

METHODS

Synthesis of Au@Pt NPs and Au@Pt−Se NPs. Synthesis of Au@Pt NPs: 20 mL of the prepared Au nanoparticle solution was mixed with 8 mL of H_2PtCl_6 solution (1 mM) and heated to 80 °C with stirring. Then, 4 mL of sodium ascorbate solution (10 mM) was added dropwise while continuing to heat and stirring for 30 min. The color of the solution gradually deepened from burgundy to transparent brown. The solution was then cooled to room temperature. The resulting Au@Pt NP solution was filtered through a 0.45 μm membrane to remove bacteria and microorganisms. The filtered solution was stored at 4 °C in a refrigerator before use.

To a clean brown reaction vial protected from light, 500 μL of a 90 μM solution of CAPN2-specific peptide chain was added. While stirring, 9.5 mL of H_2O, 285 μM of 1-[3-(dimethylamino)propyl]-3-ethylcarbodiimide hydrochloride, and *N*-hydroxysuccinimide were sequentially added to the reaction vial, followed by thorough mixing for 30 min. Finally, a 360 μM solution of L-selenocysteine was added to the reaction vial, and the reaction mixture was left overnight. The resulting solution was placed in a dialysis bag and dialyzed for 48 h. The obtained peptide chain solution was then stored in a refrigerator at 4 °C for future use. To 10 mL of Au@Pt NP solution was added a 10% solution of sodium dodecyl sulfate (SDS) to achieve a final concentration of 0.1% SDS. The mixture was stirred at room temperature for 30 min (300 rpm), followed by the addition of 4 mL of dialyzed CAPN2 peptide chain solution. The mixture was continuously illuminated for 3 h (300 rpm) and then protected from light for 24 h. After the reaction, the solution was centrifuged (12 000 rpm, 10 min) to separate the target product from unreacted substances. The obtained product was washed three times with Tris−HCl (10 mM, pH 7.4) to yield the original probe solution. The dispersed probe solution in the buffer was stored at 4 °C in a refrigerator for future use. The initial concentration of the probe was determined by measuring the UV−vis absorbance of Au@Pt NPs and Au@Pt−Se NPs at 520 nm. Prior to subsequent experiments, the original probe solution was diluted to the desired experimental concentration by using Tris−HCl. Quantification of FITC-labeled peptide chains loaded onto Au@Pt NPs can be performed using a previously reported method.[40] An excess solution of selenocysteine and cysteine was added to a final concentration of 10 mM in a 1 nM solution of the NPs. This in situ reaction results in the formation of selenocysteine-substituted peptide chains. The reaction was carried out in a light-protected environment at room temperature with continuous stirring for 24 h. After centrifugation (12 000 rpm, 10 min), the supernatant was collected, and the fluorescence intensity was measured ($\lambda_{ex}/\lambda_{em}$ = 480/520 nm, voltage = 780 V). The fluorescence intensity of FITC-labeled peptide chains at different concentrations (5, 10, 15, 100, 200, and 500 nM) was determined, and a standard fluorescence curve was constructed. The number of peptide chains attached to each Au@Pt NP was calculated using the equation derived from the curve.

Stability of Au@Pt−Se NPs under Simulated Physiological Conditions. To determine the interference of GSH on Au@Pt−Se NPs, the probe stock solution was diluted to 1 nM using Tris−HCl (10 mM, pH = 7.4). Two experimental groups were set up: one with the addition of 5 mM GSH and the other as a control group without GSH. Both groups were incubated at 37 °C for 0−12 h. The fluorescence intensity of the solution was measured every hour. Next, multiple experiments were conducted by adding GSH at concentrations of 200, 500, 1,000, and 5000 μM. After incubating the solutions at 37 °C for 12 h, the fluorescence intensity was measured.

To assess the thermal stability of Au@Pt−Se NPs, the probe solution at 1 nM concentration was incubated at various temperatures: 30, 40, 50, 60, and 70 °C for 5 min. Subsequently, the fluorescence intensity of the solutions was measured by using a fluorescence spectrophotometer, and the

https://doi.org/10.1021/acs.analchem.3c03511
Anal. Chem. 2023, 95, 18426−18435

fluorescence emission data at 520 nm were collected and plotted in a bar graph.

In Vitro Photothermal Capabilities of Au@Pt−Se NPs. To determine the photothermal effect of Au@Pt−Se NPs, different concentrations of the NP solution (0.5, 1, and 1.5 nM) and H_2O were prepared. The solutions were exposed to a 1064 nm laser at a power density of 1.8 W/cm^2 for 10 min. The temperature of the solution was monitored in real time by using a thermometer, and measurements were taken every 100 s. The experiment was repeated three times, and the average values were plotted.

For assessing the sustained photothermal effect of Au@Pt−Se NPs, a 1 nM solution of the NPs was prepared. The solution was subjected to five cycles of laser irradiation at 1064 nm with a power density of 1.8 W/cm^2. The temperature of the solution was continuously monitored by using a thermometer during each cycle of laser irradiation.

In Vitro Au@Pt−Se NP H_2O_2 to O_2 Generation. To measure the UV−vis absorption spectra of H_2O_2 at different concentrations (1, 2.5, 5, 10, 15, 20, 25, and 30 mM), UV−vis was applied within the wavelength range of 220−340 nm. The absorbance at 240 nm was recorded to construct a standard calibration curve. Subsequently, the NPs were reacted with an excess of H_2O_2. The UV−vis absorption spectra of the reaction mixture were measured at 5 min intervals for 0−30 min. The catalytic ability of Au@Pt−Se NPs to generate O_2 from H_2O_2 was evaluated. Four experimental groups were set up as follows: (1) H_2O + 0.5 μM RDPP, (2) Au@Pt−Se NPs + 0.5 μM RDPP, (3) H_2O_2 + 0.5 μM RDPP, and (4) Au@Pt−Se NPs + H_2O_2 + 0.5 μM RDPP. The fluorescence intensity was measured using a fluorescence spectrophotometer under helium protection for 0−600 s. The fluorescence intensity at 620 nm ($\lambda_{ex}/\lambda_{em}$ = 455 nm/620 nm, voltage = 650 V) was plotted.

Au@Pt−Se NPs' Responsiveness to CAPN2 Protein. To determine the optimal reaction time for the probe with CAPN2, the reaction system was prepared by adding CAPN2 at a final concentration of 1 μg/mL. After being mixed, the mixture was incubated at 37 °C in a constant temperature incubator for 0−60 min. The fluorescence signal was measured using a fluorescence spectrophotometer (5, 10, 20, 30, 35, 40, 50, and 60 min), and the standard linear calibration curve was plotted to present the changes in fluorescence intensity over time. To investigate the concentration response of Au@Pt−Se NPs with CAPN2 protein under simulated physiological conditions, a 1 nM Au@Pt−Se NP solution was reacted with different concentrations (50, 200, 400, 600, 800, and 1000 ng/mL) of CAPN2, followed by incubation at 37 °C for 35 min. The fluorescence signal was measured using a fluorescence spectrophotometer, and the standard linear calibration curve was plotted to illustrate the changes in fluorescence intensity with respect to the CAPN2 concentration.

To assess the stability of Au@Pt−Se NPs at different pH values and their response to CAPN2 protein, the probe was diluted with Tris−HCl of varying pH (10 mM, pH = 6.0, 6.4, 6.8, 7.0, 7.2, 7.4, 7.6, 7.8, and 8.0). Two parallel experiments were set up as follows: the experimental group mixed the probe with CAPN2 protein at a final concentration of 1 μg/mL, while in the control group, an equivalent volume of Tris−HCl with the corresponding pH was added. Both groups were incubated at 37 °C for 35 min. The fluorescence signal at 520 nm was collected using a fluorescence spectrophotometer, and a bar chart was plotted to compare the fluorescence intensity.

Under simulated physiological conditions, the NPs' response in the presence of the CAPN2 protease inhibitor ALLN was observed. Two groups were set up as follows: in the experimental group, the probe was mixed with ALLN solution at a final concentration of 1 μg/mL, along with CAPN2 enzyme solution at a concentration of 1 μg/mL; in the control group, only CAPN2 enzyme solution at a concentration of 1 μg/mL was added to the probe. Both groups were incubated at 37 °C for 35 min. After the reaction, the fluorescence spectra of the probe solutions in both groups were scanned by using a fluorescence spectrophotometer.

In the selectivity experiment of Au@Pt−Se NPs, different concentrations of various proteins were added to the final concentration of the 1 nM NP solution. The proteins were caspase-1, caspase-9, GSH, human neutrophil elastase, prostate-specific antigen, and CAPN2. Except for the different enzyme types added, all other conditions were kept constant. The solutions were incubated at 37 °C for 35 min, and the fluorescence signal at 520 nm was collected for each sample.

Intracellular Au@Pt−Se NPs' Specific Responsiveness to CAPN2 Protein. To further investigate the selectivity of Au@Pt−Se NPs toward tumor cells and normal cells, one group of Beas-2b cells and two groups of A549 cells were seeded in confocal culture dishes and cultured for 24 h to allow cell attachment. One group of Beas-2b cells and one group of A549 cells were treated with a culture medium containing ionomycin (a calcium ionophore), while the other group of A549 cells was pretreated with ALLN (a CAPN2 inhibitor) in the culture medium for 10 min before ionomycin treatment. After 1 h, all three groups of cells were exposed to a culture medium containing 1 nM Au@Pt−Se NPs for 4 h. The cells were then washed three times with PBS and incubated with Hoechst 33342 for 30 min. Following three additional washes with PBS, confocal imaging was performed, and the fluorescence intensity within the cells was quantified using ImageJ software.

Au@Pt−Se NPs' Performance in Hypoxia. First, the intracellular oxygen production of Au@Pt−Se NPs was investigated. A549 cells were seeded in four confocal culture dishes and cultured for 24 h to allow cell attachment. The four culture dishes were subjected to four different treatments: (1) serum +15 μM RDPP; (2) Au@Pt−Se NPs + 15 μM RDPP; (3) H_2O_2 + 15 μM RDPP; and (4) Au@Pt−Se NPs + H_2O_2 + 15 μM RDPP. After the treatments, the cells were incubated under anaerobic conditions for 4 h. Subsequently, the cells were washed three times with PBS and subjected to CLSM imaging.

To investigate the expression levels of intracellular HIF-1α, A549 cells were seeded in three confocal culture dishes and cultured for 24 h to allow cell attachment. In the first group, cells were cultured under normal O_2 conditions after the addition of Au@Pt−Se NPs. In the second group, cells were cultured under hypoxic conditions after the addition of Au@Pt−Se NPs. In the third group, cells were cultured under hypoxic conditions after the addition of Au@Pt−Se NPs and 100 μM of H_2O_2. After 4 h, the cells were washed three times with PBS. The concentration of HIF-1α was then measured using an ELISA kit.

Au@Pt−Se NPs' PTT Intracellular Performance. To investigate the PTT effect of Au@Pt−Se NPs in cells, we seeded A549 cells in six confocal culture dishes and cultured for 24 h to allow cell attachment. After incubating under hypoxic conditions for 4 h, the cells were then subjected to six

https://doi.org/10.1021/acs.analchem.3c03511
Anal. Chem. 2023, 95, 18426−18435

different treatments: (1) the control group; (2) H_2O_2 (100 μM); (3) Au@Pt−Se NPs; (4) 1064 nm laser irradiation (1.8 W/cm^2, 10 min); (5) Au@Pt−Se NPs + 1064 nm laser irradiation (1.8 W/cm^2, 10 min); and (6) Au@Pt−Se NPs + 1064 nm laser irradiation (1.8 W/cm^2, 10 min) + H_2O_2 (100 μM). The cells were washed three times with PBS, and then Calcein AM/PI staining was performed for 30 min before imaging by CLSM. Using the same treatment methods, A549 cells were seeded in five confocal culture dishes and cultured for 24 h to allow for cell attachment. The cells were subjected to five different treatments: (1) the control group; (2) H_2O_2 (100 μM); (3) Au@Pt−Se NPs; (4) 1064 nm laser irradiation (1.8 W/cm^2, 10 min); and (5) Au@Pt−Se NPs + 1064 nm laser irradiation (1.8 W/cm^2, 10 min) + H_2O_2 (100 μM). After incubation under normoxic conditions for 4 h, the cells were washed three times with PBS. Calcein AM/PI staining was performed for 30 min, and the cells were imaged using a confocal microscope.

■ ASSOCIATED CONTENT

Supporting Information

The Supporting Information is available free of charge at https://pubs.acs.org/doi/10.1021/acs.analchem.3c03511.

Experimental details, EDX spectrum of the Au@Pt NPs, DLS and TEM image of the Au@Pt-Se NPs, calibration curve between the concentration of the FITC-labeled peptide and its fluorescence intensity, stability test of the NPs in different concentrations of GSH, fluorescence excitation and mission of the Au@Pt-Se NPs reacting with CAPN2, linear calibration curve, UV-vis absorption spectra, concentration of O_2 in Au@Pt NPs with/out H_2O_2, fluorescence distribution images, and flow cytometry analysis of A549 cells (PDF)

■ AUTHOR INFORMATION

Corresponding Authors

Lili Tong − *College of Chemistry, Chemical Engineering and Materials Science, Collaborative Innovation Center of Functionalized Probes for Chemical Imaging in Universities of Shandong, Key Laboratory of Molecular and Nano Probes, Ministry of Education, Shandong Provincial Key Laboratory of Clean Production of Fine Chemicals, Shandong Normal University, Jinan 250014, P. R. China*; Email: lilitong@sdnu.edu.cn

Xiaonan Gao − *College of Chemistry, Chemical Engineering and Materials Science, Collaborative Innovation Center of Functionalized Probes for Chemical Imaging in Universities of Shandong, Key Laboratory of Molecular and Nano Probes, Ministry of Education, Shandong Provincial Key Laboratory of Clean Production of Fine Chemicals, Shandong Normal University, Jinan 250014, P. R. China*; orcid.org/0000-0002-8939-7600; Email: gaox@sdnu.edu.cn

Bo Tang − *College of Chemistry, Chemical Engineering and Materials Science, Collaborative Innovation Center of Functionalized Probes for Chemical Imaging in Universities of Shandong, Key Laboratory of Molecular and Nano Probes, Ministry of Education, Shandong Provincial Key Laboratory of Clean Production of Fine Chemicals, Shandong Normal University, Jinan 250014, P. R. China; Laoshan Laboratory, Qingdao 266237 Shandong, P. R. China*; orcid.org/0000-0002-8712-7025; Email: tangb@sdnu.edu.cn

Authors

Zixuan Chang − *College of Chemistry, Chemical Engineering and Materials Science, Collaborative Innovation Center of Functionalized Probes for Chemical Imaging in Universities of Shandong, Key Laboratory of Molecular and Nano Probes, Ministry of Education, Shandong Provincial Key Laboratory of Clean Production of Fine Chemicals, Shandong Normal University, Jinan 250014, P. R. China*

Tianrun Niu − *College of Chemistry, Chemical Engineering and Materials Science, Collaborative Innovation Center of Functionalized Probes for Chemical Imaging in Universities of Shandong, Key Laboratory of Molecular and Nano Probes, Ministry of Education, Shandong Provincial Key Laboratory of Clean Production of Fine Chemicals, Shandong Normal University, Jinan 250014, P. R. China*

Qinghao Shao − *College of Chemistry, Chemical Engineering and Materials Science, Collaborative Innovation Center of Functionalized Probes for Chemical Imaging in Universities of Shandong, Key Laboratory of Molecular and Nano Probes, Ministry of Education, Shandong Provincial Key Laboratory of Clean Production of Fine Chemicals, Shandong Normal University, Jinan 250014, P. R. China*

Junming Yue − *College of Chemistry, Chemical Engineering and Materials Science, Collaborative Innovation Center of Functionalized Probes for Chemical Imaging in Universities of Shandong, Key Laboratory of Molecular and Nano Probes, Ministry of Education, Shandong Provincial Key Laboratory of Clean Production of Fine Chemicals, Shandong Normal University, Jinan 250014, P. R. China*

Hanbo Zhang − *College of Chemistry, Chemical Engineering and Materials Science, Collaborative Innovation Center of Functionalized Probes for Chemical Imaging in Universities of Shandong, Key Laboratory of Molecular and Nano Probes, Ministry of Education, Shandong Provincial Key Laboratory of Clean Production of Fine Chemicals, Shandong Normal University, Jinan 250014, P. R. China*

Complete contact information is available at: https://pubs.acs.org/10.1021/acs.analchem.3c03511

Author Contributions

[§]Z. C. and T. N. contribute equally to this work. All authors have given approval to the final version of the manuscript.

Notes

The authors declare no competing financial interest.

■ ACKNOWLEDGMENTS

This work was supported by the National Natural Science Foundation of China (22134004), the Natural Science Foundation of Shandong Province (ZR2020MB109), the Major Science and Technology Innovation Project of Shandong Province (2021ZDSYS09), and the Local Science and Technology Development Fund Guided by the Central Government of Shandong Province (YDZX2022012).

■ REFERENCES

(1) Neal, R. D.; Sun, F.; Emery, J. D.; Callister, M. E. *BMJ* **2019**, *365*, l1725.
(2) Testa, U.; Castelli, G.; Pelosi, E. *Cancers* **2018**, *10*, 248.
(3) Thai, A. A.; Solomon, B. J.; Sequist, L. V.; Gainor, J. F.; Heist, R. S. *Lancet* **2021**, *398*, 535−554.
(4) Nooreldeen, R.; Bach, H. *Int. J. Mol. Sci.* **2021**, *22*, 8661.
(5) Ngo, P.; Pinkston, C. M.; Kloecker, G. H. *J. Clin. Oncol.* **2019**, *37*, 146.

(6) Giaccone, G.; He, Y. *Semin. Cancer Biol.* **2023**, *94*, 1−10.
(7) Calvo-Lozano, O.; García-Aparicio, P.; Raduly, L.-Z.; Estévez, M. C.; Berindan-Neagoe, I.; Ferracin, M.; Lechuga, L. M. *Anal. Chem.* **2022**, *94*, 14659−14665.
(8) Salem, A.; Asselin, M.-C.; Reymen, B.; Jackson, A.; Lambin, P.; West, C. M. L.; O'Connor, J. P. B.; Faivre-Finn, C. *J. Natl. Cancer Inst.* **2018**, *110*, 14−30.
(9) Park, Y. I.; Kwon, S.-H.; Lee, G.; Motoyama, K.; Kim, M. W.; Lin, M.; Niidome, T.; Choi, J. H.; Lee, R. *J. Controlled Release* **2021**, *330*, 1−14.
(10) Peng, X. L.; Yang, R.; Song, J.; Wang, X.; Dong, W. G. *Front. Med.* **2022**, *9*, 14.
(11) Balata, H.; Quaife, S. L.; Craig, C.; Ryan, D. J.; Bradley, P.; Crosbie, P. A. J.; Murray, R. L.; EVison, M. *Clin. Oncol.* **2022**, *34*, 708−715.
(12) Fitzgerald, R. C.; Antoniou, A. C.; Fruk, L.; Rosenfeld, N. *Nat. Med.* **2022**, *28*, 666−677.
(13) Harjes, U. *Nat. Rev. Cancer* **2017**, *17*, 708.
(14) Pashayan, N.; Pharoah, P. D. P. *Science* **2020**, *368*, 589−590.
(15) Yuan, C.-S.; Deng, Z.-W.; Qin, D.; Mu, Y.-Z.; Chen, X.-G.; Liu, Y. *Acta Biomater.* **2021**, *125*, 1−28.
(16) Gai, L.; Liu, Y.; Zhou, Z.; Lu, H.; Guo, Z. *Coord. Chem. Rev.* **2023**, *481*, 215041.
(17) Chen, H.; Tian, J.; He, W.; Guo, Z. *J. Am. Chem. Soc.* **2015**, *137*, 1539−1547.
(18) Shi, T.; Huang, C.; Li, Y.; Huang, F.; Yin, S. *Biomaterials* **2022**, *285*, 121535.
(19) Wang, W.; Zheng, H.; Jiang, J.; Li, Z.; Jiang, D.; Shi, X.; Wang, H.; Jiang, J.; Xie, Q.; Gao, M.; Chu, J.; Cai, X.; Xia, T.; Li, R. *Nat. Commun.* **2022**, *13*, 4495.
(20) Shen, F.; Zhang, C.; Cai, Z.; Wang, J.; Zhang, X.; Machuki, J. O. a.; Shi, H.; Gao, F. *Anal. Chem.* **2020**, *92*, 16158−16169.
(21) Feng, W.; Han, X.; Wang, R.; Gao, X.; Hu, P.; Yue, W.; Chen, Y.; Shi, J. *Adv. Mater.* **2019**, *31*, No. e1805919.
(22) Chen, Y.; Li, D.; Zhong, Y.; Lu, Z.; Wang, D. *Int. J. Biol. Macromol.* **2023**, *235*, 123683.
(23) Wang, W.; Ma, E.; Tao, P.; Zhou, X.; Xing, Y.; Chen, L.; Zhang, Y.; Li, J.; Xu, K.; Wang, H.; Zheng, S. *J. Mater. Sci. Technol.* **2023**, *148*, 171−185.
(24) Liu, F.; Gong, S.; Shen, M.; He, T.; Liang, X.; Shu, Y.; Wang, X.; Ma, S.; Li, X.; Zhang, M.; Wu, Q.; Gong, C. *Chem. Eng. J.* **2021**, *403*, 126305.
(25) Cai, R.; Xiang, H.; Yang, D.; Lin, K.-T.; Wu, Y.; Zhou, R.; Gu, Z.; Yan, L.; Zhao, Y.; Tan, W. *J. Am. Chem. Soc.* **2021**, *143*, 16113−16127.
(26) Dai, H.; Wang, X.; Shao, J.; Wang, W.; Mou, X.; Dong, X. *Small* **2021**, *17*, No. e2102646.
(27) Sharma, H.; Mishra, P. K.; Talegaonkar, S.; Vaidya, B. *Drug Discovery Today* **2015**, *20*, 1143−1151.
(28) Hu, B.; Kong, F.; Gao, X.; Jiang, L.; Li, X.; Gao, W.; Xu, K.; Tang, B. *Angew. Chem., Int. Ed.* **2018**, *57*, 5306−5309.
(29) Gao, X.; Jiang, L.; Hu, B.; Kong, F.; Liu, X.; Xu, K.; Tang, B. *Anal. Chem.* **2018**, *90*, 4719−4724.
(30) Liu, X.; Liu, J.; Xu, S.; Li, X.; Wang, Z.; Gao, X.; Tang, B.; Xu, K. *ACS Appl. Mater. Interfaces* **2023**, *15*, 2529−2537.
(31) Liu, X.; Zhang, X.; Zhu, M.; Lin, G.; Liu, J.; Zhou, Z.; Tian, X.; Pan, Y. *ACS Appl. Mater. Interfaces* **2017**, *9*, 279−285.
(32) Iglesias-Mayor, A.; Amor-Gutiérrez, O.; Novelli, A.; Fernández-Sánchez, M. T.; Costa-García, A.; de la Escosura-Muñiz, A. *Anal. Chem.* **2020**, *92*, 7209−7217.
(33) Jung, N.; Sohn, Y.; Park, J. H.; Nahm, K. S.; Kim, P.; Yoo, S. J. *Appl. Catal., B* **2016**, *196*, 199−206.
(34) Chen, Y.-Z.; Wang, Z. U.; Wang, H.; Lu, J.; Yu, S.-H.; Jiang, H.-L. *J. Am. Chem. Soc.* **2017**, *139*, 2035−2044.
(35) Xiang, Z.-P.; Tan, A.-D.; Fu, Z.-Y.; Piao, J.-H.; Liang, Z.-X. *J. Energy Chem.* **2020**, *49*, 323−326.
(36) Yu, J.; Liu, S.; Wang, Y.; He, X.; Zhang, Q.; Qi, Y.; Zhou, D.; Xie, Z.; Li, X.; Huang, Y. *Bioact.Mater.* **2022**, *7*, 389−400.
(37) Zhang, C.; Qin, W.-J.; Bai, X.-F.; Zhang, X.-Z. *Nano Today* **2020**, *35*, 100960.
(38) March-Diaz, R.; Lara-Ureña, N.; Romero-Molina, C.; Heras-Garvin, A.; Ortega-de San Luis, C.; Alvarez-Vergara, M. I.; Sanchez-Garcia, M. A.; Sanchez-Mejias, E.; Davila, J. C.; Rosales-Nieves, A. E.; Forja, C.; Navarro, V.; Gomez-Arboledas, A.; Sanchez-Mico, M. V.; Viehweger, A.; Gerpe, A.; Hodson, E. J.; Vizuete, M.; Bishop, T.; Serrano-Pozo, A.; Lopez-Barneo, J.; Berra, E.; Gutierrez, A.; Vitorica, J.; Pascual, A. *Nat. Aging* **2021**, *1*, 385−399.
(39) Xia, H.; Xiahou, Y.; Zhang, P.; Ding, W.; Wang, D. *Langmuir* **2016**, *32*, 5870−5880.
(40) Gao, X.; Niu, T.; Xia, Q.; Hu, B.; Zhao, Z.; Feng, X.; Yang, J.; Tang, B.; Xu, K. *Anal. Chim. Acta* **2022**, *1210*, 339852.

https://doi.org/10.1021/acs.analchem.3c03511
Anal. Chem. 2023, 95, 18426−18435